Loss Difference Induced Localization in a Non-Hermitian Honeycomb Photonic Lattice

Yuan Feng,[1,*] Zhenzhi Liu,[1,*] Fu Liu,[1,†] Jiawei Yu,[1] Shun Liang,[1] Feng Li,[1] Yanpeng Zhang,[1] Min Xiao,[2,3] and Zhaoyang Zhang[1,‡]

[1]*Key Laboratory for Physical Electronics and Devices of the Ministry of Education & Shaanxi Key Lab of Information Photonic Technique, School of Electronic Science and Engineering, Faculty of Electronic and Information Engineering, Xi'an Jiaotong University, Xi'an 710049, China*

[2]*Department of Physics, University of Arkansas, Fayetteville, Arkansas 72701, USA*

[3]*National Laboratory of Solid State Microstructures and School of Physics, Nanjing University, Nanjing 210093, China*

(Received 7 November 2022; accepted 25 May 2023; published 6 July 2023)

Non-Hermitian systems with complex-valued energy spectra provide an extraordinary platform for manipulating unconventional dynamics of light. Here, we demonstrate the localization of light in an instantaneously reconfigurable non-Hermitian honeycomb photonic lattice that is established in a coherently prepared atomic system. One set of the sublattices is optically modulated to introduce the absorptive difference between neighboring lattice sites, where the Dirac points in reciprocal space are extended into dispersionless local flat bands, with two shared eigenstates: low-loss (high-loss) one with fields confined at sublattice B (A). When these local flat bands are broad enough due to larger loss difference, the incident beam with its tangential wave vector being at the K point in reciprocal space is effectively localized at sublattice B with weaker absorption, namely, the commonly seen power exchange between adjacent channels in photonic lattices is effectively prohibited. The current work unlocks a new capability from non-Hermitian two-dimensional photonic lattices and provides an alternative route for engineering tunable local flat bands in photonic structures.

DOI: 10.1103/PhysRevLett.131.013802

Loss is usually considered to be detrimental for wave manipulations as it leads to energy decay. However, since the introduction of non-Hermitian physics within the context of quantum field theories into optical and other systems, the combination of dispersion and loss in desired manners has inspired considerable new phenomena, particularly, the unusual wave dynamical characteristics arising from the complex-valued eigenvalue spectra [1–7], such as non-Hermitian topological properties [8–10], non-Hermitian skin effect [11,12], lasing and optical sensing [13,14], etc. Most of the counterintuitive features in non-Hermitian optical settings [15–20] are closely related to the well-known exceptional points (EPs) [21,22], around which the complex eigenvalues or band structures undergo bifurcation and an abrupt phase transition occurs. To date, the studies of non-Hermitian potentials have been extended to the high-dimensional framework, where exceptional rings (ERs) emerge in momentum space, inside which local flat bands (LFBs) become possible [18,19,23,24]. These pioneering works mainly focused on the exotic wave dynamics around ERs by manipulating the degree of non-Hermiticity.

Recently, LFBs inside ERs are theoretically proposed to govern the behaviors of light in distinct manners, for example, chiroptical polarization response [25]. Expanding the research interests from the vicinity of ERs to the ring-surrounded areas will further enrich the capabilities and applications of high-dimensional non-Hermitian systems. Nevertheless, the experimental explorations on the underlying properties inside ERs are rarely reported.

One intrinsic property of the dispersionless flat band (FB) is to realize field localization. In general, the localization of optical field in periodic photonic structures is achieved by taking advantage of energy FBs in the whole Brillouin zone [26] and quasi-energy band collapse with modulation [27,28], such as the localizations in one-dimensional (1D) photonic chain [29], photonic Lieb and Kagome lattices [26,30,31], moiré superlattices [32], among others. This is because the nondispersive FB guarantees zero group velocity, therefore the wave packet will propagate in a dispersionless manner through media. However, it is not always necessary to have an entire FB for the field localization, as the Fourier components of the wave packet usually cover part of the momentum space, rather than the whole $\boldsymbol{k}$ space.

In this Letter, we experimentally demonstrate the field localization in a non-Hermitian honeycomb photonic lattice (HPL). Such localization of the incident beam into one subset of the lattice results from the LFBs (around the K and K' points) that are induced by the loss difference (LDF)

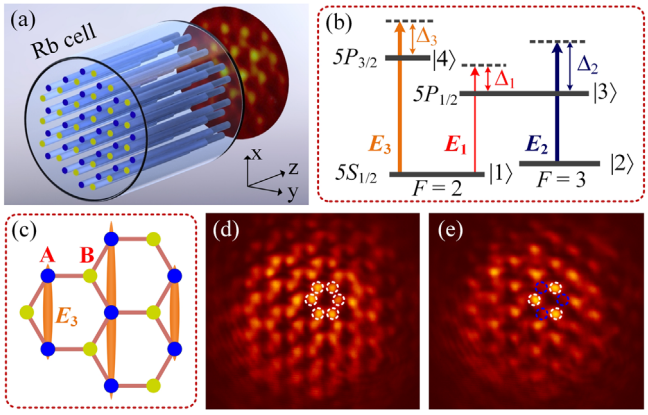

FIG. 1. (a) Experimental sketch. (b) The four-level ^{85}Rb atomic configuration. (c) The spatial arrangements of the pump field $\boldsymbol{E}_3$ and the HPL inside the medium. (d)–(e) The observed output probe patterns without and with A sublattice covered by $\boldsymbol{E}_3$, respectively.

between the two sublattices. The HPL is constructed in a four-level N-type ^{85}Rb atomic vapor cell with electromagnetically induced transparency (EIT) [33]. The instantaneous reconfigurability of such HPL supports the demonstration of the dynamical behaviors of the wave packets by setting different experimental parameters. The HPL with the same complex refractive index for all lattice sites is "written" by a coupling field with a hexagonal intensity distribution under EIT in a three-level configuration [34–36]. The incident Gaussian probe beam is discretized into the honeycomb geometry by the HPL, and the light in two neighboring channels (corresponding to A and B sites) can experience power exchange due to evanescent coupling. With the introduction of another 1D periodic pump field to cover one set of sublattice [for example, the A sublattice, see Figs. 1(a) and 1(c)] in the HPL, a four-level system is formed at the covered regions. Namely, the susceptibilities of A and B sublattices are governed by the interactions between the probe beam and four- and three-level atomic configurations, respectively, leading to different transmission characteristics for the light inside corresponding waveguides. When the LDF between A and B sites is large enough by changing the detuning of the 1D field, there emerge the LFBs that can localize the fields at one set of sublattice, suppressing the energy exchange between neighboring lattice sites. Such LDF-induced LFB exhibits the similar zero-dispersion property as commonly seen in FB structures such as Lieb lattices [30,31]. The current work confirms the loss guiding or localization effect, acting as the counterpart of gain guiding effect [37], and advocates a novel application of loss, which is naturally present but generally unwanted in optics.

The experimental principle is schematically shown in Fig. 1(a), where the honeycomb refractive index distribution inside the vapor cell is optically induced by a coupling field $\boldsymbol{E}_2$ with a hexagonal intensity profile (by interfering three coupling beams) under EIT. According to the transient properties of EIT [38], the characteristic scale of the switching time of the EIT-based HPL is several nanoseconds. The lattice sites with different colors correspond to the HPL's A and B sublattices. A Gaussian probe field $\boldsymbol{E}_1$ is launched into the cell from the same side as $\boldsymbol{E}_2$ to excite one K valley, while the directions of the three coupling beams identify three K' points in the reciprocal space. A 1D periodic pump field $\boldsymbol{E}_3$ by interfering two pump beams is injected to cover the A sublattice. See more details of experimental settings in the Supplemental Material [39].

As given in Fig. 1(b), the probe and coupling fields ($\boldsymbol{E}_1$ and $\boldsymbol{E}_2$) drive the three-level configuration $|1\rangle \rightarrow |3\rangle \rightarrow |2\rangle$, in which an EIT window occurs to enhance the refractive index felt by $\boldsymbol{E}_1$. $\boldsymbol{E}_3$ drives the transition $|1\rangle \rightarrow |4\rangle$ to excite a four-level configuration (only at A sites), which can lead to different absorptions for the two sets of sublattice. Detuning Δ_i ($i = 1$, 2, and 3) represents the difference between the laser frequency and the frequency gap of the two levels connected by $\boldsymbol{E}_i$. The spatial beam arrangement of the pump field and HPL is shown in Fig. 1(c). For the three-level EIT case, the resulted refractive index is inversely related to the coupling-field intensity. With the two-photon detuning set as $\Delta_1 - \Delta_2 > 0$, the reconfigurable non-Hermitian HPL with honeycomb real and imaginary parts is effectively established [43]. The transmitted probe pattern (at the output surface of the cell and captured by a charge coupled device camera) from the uniform susceptibility for both sublattices is shown in Fig. 1(d), which exhibits a discrete honeycomb pattern. With $\boldsymbol{E}_3$ introduced to modulate the imaginary part of A sublattice, the transmitted intensity [Fig. 1(e)] at A sites (marked by blue dashed circles) is much weaker due to the larger imaginary part (representing stronger absorption).

One advantage of the induced HPL is the easily accessible tunability inherited from the multilevel atomic system. Here, we show that LDF between the A and B sites of the non-Hermitian HPL can be controlled by laser parameters. Figures 2(a)–2(f) demonstrate the evolutions of the output intensity at A (blue circles) and B (white circles) sublattices versus pump-field detuning Δ_3 (which only affects the susceptibility of A sites) under normal incidence. With Δ_3 tuned from 120 to 20 MHz, the absorption experienced in A sites becomes stronger, resulting in a decrease of the intensity inside blue circles, while the intensity at uncovered B sites exhibits unnoticeable change. These observations demonstrate the increase of LDF between A and B sublattices with decreasing Δ_3.

The interaction between the probe beam and the four-level atomic configuration can be described by the density matrix method [39,44], according to which the loss parameters $\gamma_{a,b} = \mathrm{Im}[\chi_{a,b}]$ at the A and B sites are plotted

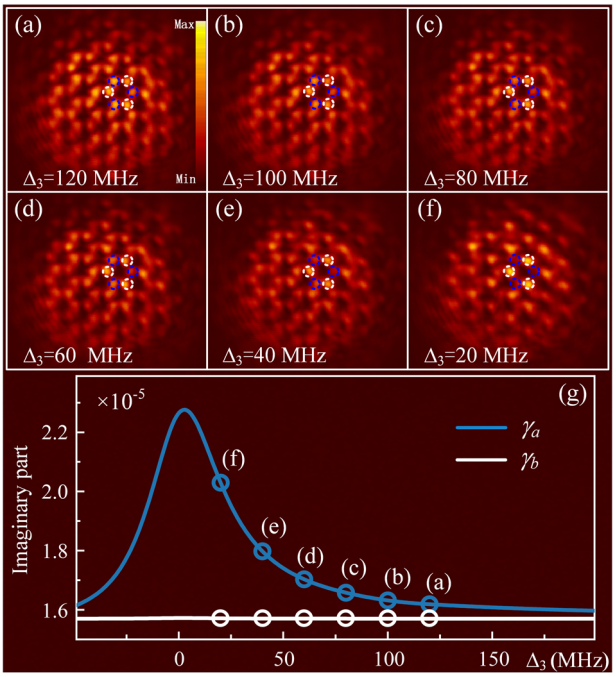

FIG. 2. (a)–(f) Output patterns by changing Δ_3 from 120 to 20 MHz with $\Delta_1 - \Delta_2 = 25$ MHz; (g) the calculated imaginary parts of the susceptibility at the A and B sites. The six symbols correspond to the detunings in (a)–(f).

in Fig. 2(g), with symbols denoting the detunings corresponding to Figs. 2(a)–2(f). When Δ_3 is tuned from 120 to 20 Mhz, γ_b keeps constant while γ_a increases, resulting in the enlargement of LDF $\Delta\gamma = \gamma_a - \gamma_b$. The estimated LDF values of Figs. 2(a)–2(f) are $\Delta\gamma = 0.49$, 0.62, 0.88, 1.33, 2.27, and $4.59(\times 10^{-6})$, respectively. This result advocates the instantaneous reconfigurability of the established HPL, which provides a tunable platform to govern the non-Hermitian-related wave dynamics.

Such a non-Hermitian HPL system can be described by the effective tight-binding model with Hamiltonian [45,46]

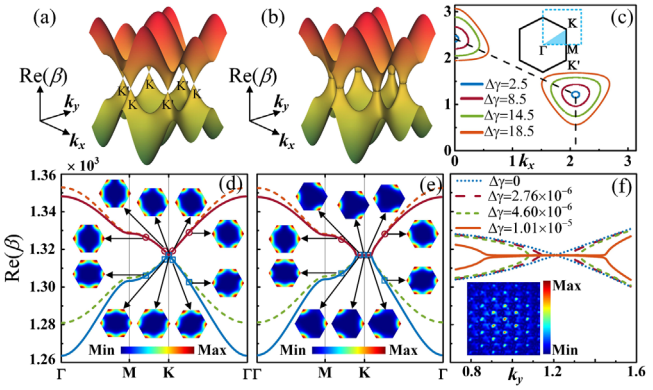

FIG. 3. Calculated band structures and eigenstates of the non-Hermitian HPL. (a),(b) Bands of Re$[\beta]$ according to Eq. (2) for $\Delta\gamma = 0$ (a) and $\Delta\gamma = 8.5$ (b) with $\kappa = 12$. n_0 and $(\gamma_a + \gamma_b)/2$ can be set arbitrarily as they only shift the bands up or down. (c) Boundaries of the LFBs for different $\Delta\gamma$. The inset shows the first Brillouin zone. (d),(e) Band structures (solid lines) with $\Delta\gamma = 0$ (d) and $\Delta\gamma = 4.1 \times 10^{-6}$ (e), together with representative eigenstates (insets). The dashed lines are the corresponding bands in Eq. (2) from the analytic tight-binding model for comparison. (f) Evolutions of the LFB around one K point by increasing $\Delta\gamma$. The inset shows the localized field pattern when the LFB (LDF) is large enough.

$$\mathbf{H} = \begin{pmatrix} n_a & \kappa \sum_m e^{i\boldsymbol{k}\cdot\boldsymbol{r}_m} \\ \kappa \sum_m e^{-i\boldsymbol{k}\cdot\boldsymbol{r}_m} & n_b \end{pmatrix}, \tag{1}$$

where $n_{a,b} = n_0 - i\gamma_{a,b}$ are the normalized complex refractive indices at A and B sites, κ is the normalized coupling strength between neighboring sites, $\boldsymbol{k} = (k_x, k_y)$ is the two-dimensional wave number, and $\boldsymbol{r}_{1,2,3} = (1, 0)$, $(-\frac{1}{2}, \sqrt{3}/2)$, $(-\frac{1}{2}, -\sqrt{3}/2)$ are the normalized coupling directions on the x-y plane. The eigenvalues of this Hamiltonian, which characterize the propagation properties of the probe beam inside the system, are found to be

$$\beta_{1,2} = n_0 - \frac{1}{2} i(\gamma_a + \gamma_b) \pm \kappa \sqrt{3 - \left(\frac{\Delta\gamma}{2\kappa}\right)^2 + 2\left(2\cos\frac{3k_x}{2}\cos\frac{\sqrt{3}k_y}{2} + \cos(\sqrt{3}k_y)\right)}. \tag{2}$$

When $\Delta\gamma = \gamma_a - \gamma_b = 0$, such eigenvalues can be visualized in the band structure [Fig. 3(a)]. It is obvious that they degenerate at the Dirac points (K and K' points, real part of the eigenvalues) and locally show linear dispersion properties. However, when $\Delta\gamma \neq 0$, the point degeneracy becomes circular-surface-like degeneracy and the original linear dispersion evolves into local dispersionless FB around K and K' points. This can be seen in the band structure of Re$[\beta]$ in Fig. 3(b) for $\Delta\gamma = 8.5$ and $\kappa = 12$ (normalized parameters). The corresponding bands of Im$[\beta]$ (which is dispersive but produces minor filtering effect) are shown and analyzed in Fig. S4(a) in Supplemental Material [39]. Such a LFB surface can localize the incident light due to locally zero group velocity. Moreover, in Fig. 3(c), we plot the boundaries of the LFBs for different $\Delta\gamma$. With the increase of $\Delta\gamma$, the LFB surfaces become broader, enabling better localization.

The formation of the LFB under nonzero LDF can be understood from the Dirac Hamiltonian approximation

around K and K' points. By taking the Taylor series expansion of Eq. (1), one can obtain

$$\mathbf{H}_D = \begin{pmatrix} n_0 - i\gamma_a & \kappa' k e^{i\theta} \\ \kappa' k e^{-i\theta} & n_0 - i\gamma_b \end{pmatrix}, \tag{3}$$

where $\kappa' = 3\kappa/2$, k is the amplitude of the wave number reference to the K (K') point, and θ is the local direction angle. The eigenvalues are

$$\beta_{1,2} = n_0 - \frac{1}{2} i(\gamma_a + \gamma_b) \pm \kappa' \sqrt{k^2 - \left(\frac{\Delta\gamma}{2\kappa'}\right)^2}. \tag{4}$$

Now, the degeneracy condition $k^2 - (\Delta\gamma/2\kappa')^2 = 0$ is dependent on the amplitude of the local wave number k, indicating that the degenerate point evolves to an ER [23,47]. In addition, the size of ERs and LFBs (real part of the eigenvalues) increases proportionally to $\Delta\gamma$ [Fig. 3(c)].

We calculate the band structures [the solid lines in Figs. 3(d) and 3(e)] of the synthesized HPL using the PDE module of COMSOL Multiphysics. One can see that the Dirac cone at the K point for $\Delta\gamma = 0$ becomes LFB for $\Delta\gamma = 4.1 \times 10^{-6}$, agreeing with the analytic results (dashed lines) of Eq. (2) from the tight-binding model, especially in the vicinity of K points. We note that the minor difference between band structures close to Γ point based on the two methods is due to the simplicity of the symmetric tight-binding model. To better demonstrate the formation of the LFBs, in Fig. 3(f), we plot the bands around K point for different $\Delta\gamma$. With the increase of the $\Delta\gamma$, the LFB expands broader. Also, we show representative eigenstates in the inset of Figs. 3(d) and 3(e). It is worth noting that, with the increase $\Delta\gamma$, the LFBs not only emerge and expand, but also share the similar eigenstates for each band. Particularly, for the eigenstates of the upper (lower) LFB, the field is localized at B (A) sites with low (high) loss. When a probe beam is obliquely incident into the system to excite the K vicinity, the eigenstates of both LFBs will be excited. However, since the B lattice sites have lower loss, the eigenstates of field concentrated at A sites (lower band) will decay much faster and finally only the upper band survives, resulting in the field localization at B sites. The inset of Fig. 3(f) shows the simulated localized field pattern for a certain propagating distance in the synthetic HPL with a relatively large LDF. The probe beam will keep this localized profile when propagating inside the lattice but experience the amplitude decay due to the loss.

In experiment, the field localization can be verified by examining the energy exchange between A and B sites. For a large enough LDF, the field can be localized at B sites and there should be no energy transportation between A and B sites. While the field fails to be localized for a relatively small LDF, the energy at A and B sites will couple to each other and resulting in energy fluctuations. Here we show the observed energy exchange between two adjacent waveguides (corresponding to A and B sublattices) at different $\Delta\gamma$. One advantage of atomic media is that increasing the atomic density (positively related to the temperature of the vapors) is understood as extending the effective propagating distance of the probe beam inside the HPL [34,48]. With Δ_3 adjusted to establish different LDF, the dynamics of the probe beam are captured in Fig. 4 with the medium heated from 120 °C to 165 °C. Actually, considering that the susceptibility is proportional to the atomic density N for the current configuration [Eq. (S2) in Supplemental Material [39]], higher temperature can cause a larger imaginary part as well as larger $\Delta\gamma$, which will result in weaker transmission but the improvement of the field localization. The relatively transmitted intensities I_A and I_B at A and B sites are measured by the software of the charge coupled device camera and their proportions are represented by symbols in Fig. 4.

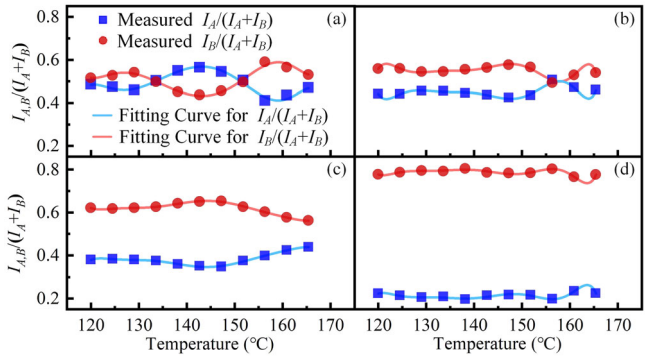

FIG. 4. Observed energy exchanges between sublattices A and B during the propagation of probe under different pump parameters: (a) without $\boldsymbol{E}_3$, (b) $\Delta_3 = 120$ MHz, (c) $\Delta_3 = 40$ MHz, and (d) $\Delta_3 = 20$ MHz. The squares and dots are the measured proportions of the transmitted intensities at the A and B sites, respectively, while the corresponding solid curves represent mathematic fitting based on the experimental measurements and provide a guide to the eye.

When $\boldsymbol{E}_3$ is absent, all the sites on the HPL possess the same susceptibility controlled by EIT. In this case, the LDF is zero ($\Delta\gamma = 0$) and the power exchange between neighboring waveguides is observed in Fig. 4(a), where the initial intensities I_A and I_B are almost the same. During the propagation, there exists twice energy exchanges indicated by the two points where $I_A \approx I_B$.

With the small increase of $\Delta\gamma$ by setting $\Delta_3 = 120$ MHz [see Fig. 2(g)], as shown in Fig. 4(b), the frequency of power exchange between the A and B sites is reduced to only once at ~155 °C, which means the energy exchange requires a longer propagating distance than the case without the pump field. The slowing down of the power exchange indicates the formation of the LFB surface but still a limited area, which cannot fully localize the beam.

With $\Delta_3 = 40$ MHz[Fig. 4(c)], the LDF is further enlarged and a broader LFB surface occurs. Consequently, there is no power exchange in the given propagation distance. For the very large LDF in Fig. 4(d) with $\Delta_3 = 20$ MHz, the ratio I_A/I_B reaches $\sim 1:4$. Since the generated LFBs have large enough areas and can confine the energy mostly in B sublattices. However, when the probe beam excites the P point (midpoint of Γ and K points), the power oscillation restores, as shown in Figs. S5 and S6 [39]. Correspondingly, we simulate the propagation dynamics in the synthetic HPL with the susceptibility distribution at the same order of magnitude as the experiment [49]. The simulations (both COMSOL simulation and tight-binding model) of the energy exchange depending on normalized propagating distance are plotted in Figs. S7 and S8 [39], which show very similar energy evolution behaviors as the experiment. Actually, by increasing the nonlinearity inside a two-waveguide system can also cause the localization effect [50–53]. However, the observed switch from localization to nonlocalization in Figs. S5 and S6 [39] advocates that nonlinearity does not play a role in the obtained localization, because such a small change on the incident angle (from $\sim 0.23°$ to $\sim 0.12°$, i.e., from the K to P point in $\boldsymbol{k}$ space) will not affect the nonlinearity of the medium.

In conclusion, we experimentally demonstrate the field localization behavior by switching the band structures from Dirac points with linear dispersion to dispersionless LFBs in a reconfigurable non-Hermitian HPL induced in multilevel atomic vapors. Such switching is derived from the induced LDF between A and B sublattices, whose susceptibility are controlled by four- and three-level atomic configurations, respectively. By easily setting the laser parameters, the imaginary part as well as the size of the formed LFB is effectively manipulated to govern the beam dynamics in individual waveguides. The occurrence of the LFB is verified by the vanishing of power exchange, indicating that the light is localized by the LFB modes. Different from the phenomena involving EPs or ERs in previous works [19,23,24], the localization of optical fields in the current work is related to the property inside the ERs by proper manipulation of LDF in the non-Hermitian system. Namely, the localization behavior arising from LDF is a result of the LFB with shared eigenstates, and does not depend on the EPs. Our work not only uncovers a new property of non-Hermitian HPLs but also opens the door for the experimental exploration on the capabilities of rings-surrounded LFBs in high-dimensional non-Hermitian systems.

In addition, the instantaneous reconfigurability on the positions of EPs in the reciprocal space can lead to remarkable properties and applications, such as the desired control on the angle of emission of the modes [54] and on the improvement of sensitivity of optical sensing [14,55–57] surrounding the EPs. Although tuning the coordinates of EPs in $\boldsymbol{k}$ space has been already realized, our work provides a platform for effectively controlling the ERs in $\boldsymbol{k}$ space. Moreover, since the output beam could be selectively guided or confined to either the A or B sublattice array as required, the obtained localization effect can find potential applications in beam-multiplexed optical communications [58].

We thank Professors Yaroslav V. Kartashov and Dmitry Solnyshkov for insightful discussions. This work was mainly supported by the National Key R&D Program of China (2018YFA0307500), the National Natural Science Foundation of China (12274339, 62022066, 12074306, 11804267), and the Key Scientific and Technological Innovation Team of Shaanxi Province (2021TD-56). Z. L. and F. L. also acknowledge the financial support from Xi'an Jiaotong University and Shaanxi Province, P. R. China.

*Y. F. and Z. L. contributed equally to this work.
†fu.liu@xjtu.edu.cn
‡zhyzhang@xjtu.edu.cn

[1] R. El-Ganainy, K. G. Makris, M. Khajavikhan, Z. H. Musslimani, S. Rotter, and D. N. Christodoulide, Non-Hermitian physics and PT symmetry, Nat. Phys. **14**, 11 (2018).
[2] M. P. Hokmabadi, A. Schumer, D. N. Christodoulides, and M. Khajavikhan, Non-Hermitian ring laser gyroscopes with enhanced Sagnac sensitivity, Nature (London) **576**, 70 (2019).
[3] Z. Zhang, Y. Zhang, J. Sheng, L. Yang, M. Miri, D. N. Christodoulides, B. He, Y. Zhang, and M. Xiao, Observation of Parity-Time Symmetry in Optically Induced Atomic Lattices, Phys. Rev. Lett. **117**, 123601 (2016).
[4] H. Nasari, G. Lopez-Galmiche, H. E. Lopez-Aviles, A. Schumer, A. U. Hassan, Q. Zhong, S. Rotter, P. LiKamWa, D. N. Christodoulides, and M. Khajavikhan, Observation of chiral state transfer without encircling an exceptional point, Nature (London) **605**, 256 (2022).
[5] A. Hashemi, K. Busch, D. N. Christodoulides, S. K. Ozdemir, and R. El-Ganainy, Linear response theory of open systems with exceptional points, Nat. Commun. **13**, 3281 (2022).
[6] H. Cao and J. Wiersig, Dielectric microcavities: Model systems for wave chaos and non-Hermitian physics, Rev. Mod. Phys. **87**, 61 (2015).
[7] V. V. Konotop, J. Yang, and D. A. Zezyulin, Nonlinear waves in PT-symmetric systems, Rev. Mod. Phys. **88**, 035002 (2016).
[8] M. Kremer, T. Biesenthal, L. J. Maczewsky, M. Heinrich, R. Thomale, and A. Szameit, Demonstration of a two-dimensional PT-symmetric crystal, Nat. Commun. **10**, 435 (2019).
[9] H. Zhao, X. Qiao, T. Wu, B. Midya, S. Longhi, and L. Feng, Non-Hermitian topological light steering, Science **365**, 1163 (2019).
[10] B. Höckendorf, A. Alvermann, and H. Fehske, Non-Hermitian Boundary State Engineering in Anomalous Floquet Topological Insulators, Phys. Rev. Lett. **123**, 190403 (2019).

[11] F. Song, S. Yao, and Z. Wang, Non-Hermitian Skin Effect and Chiral Damping in Open Quantum Systems, Phys. Rev. Lett. **123**, 170401 (2019).
[12] N. Okuma, K. Kawabata, K. Shiozaki, and M. Sato, Topological Origin of Non-Hermitian Skin Effects, Phys. Rev. Lett. **124**, 086801 (2020).
[13] B. Zhu, Q. Wang, D. Leykam, H. Xue, Q. Wang, and Y. D. Chong, Anomalous Single-Mode Lasing Induced by Nonlinearity and the Non-Hermitian Skin Effect, Phys. Rev. Lett. **129**, 013903 (2022).
[14] W. Chen, Ş. K. Özdemir, G. Zhao, J. Wiersig, and L. Yang, Exceptional points enhance sensing in an optical microcavity, Nature (London) **548**, 192 (2017).
[15] M. Pan, H. Zhao, P. Miao, S. Longhi, and L. Feng, Photonic zero mode in a non-Hermitian photonic lattice, Nat. Commun. **9**, 1308 (2018).
[16] H. Xue, Q. Wang, B. Zhang, and Y. D. Chong, Non-Hermitian Dirac Cones, Phys. Rev. Lett. **124**, 236403 (2020).
[17] A. Cerjan, M. Xiao, L. Yuan, and S. Fan, Effects of non-Hermitian perturbations on Weyl Hamiltonians with arbitrary topological charges, Phys. Rev. B **97**, 075128 (2018).
[18] E. J. Bergholtz, J. C. Budich, and F. K. Kunst, Exceptional topology of non-Hermitian systems, Rev. Mod. Phys. **93**, 015005 (2021).
[19] B. Zhen, C. W. Hsu, Y. Igarashi, L. Lu, I. Kaminer, A. Pic, S. Chua, J. D. Joannopoulos, and M. Soljačič, Spawning rings of exceptional points out of Dirac cones, Nature (London) **525**, 354 (2015).
[20] Y. Fu and S. Wan, Degeneracy and defectiveness in non-Hermitian systems with open boundary, Phys. Rev. B **105**, 075420 (2022).
[21] Z. Ren, D. Liu, E. Zhao, Ch. He, K. K. Pak, J. Li, and G. Jo, Chiral control of quantum states in non-Hermitian spin-orbit-coupled fermions, Nat. Phys. **18**, 385 (2022).
[22] J. d. Pino, J. J. Slim, and E. Verhagen, Non-Hermitian chiral phononics through optomechanically induced squeezing, Nature (London) **606**, 82 (2022).
[23] A. Cerjan, S. Huang, M. Wang, K. P. Chen, Y. Chong, and M. C. Rechtsman, Experimental realization of a Weyl exceptional ring, Nat. Photonics **13**, 623 (2019).
[24] Y. Xu, S.-T. Wang, and L.-M. Duan, Weyl Exceptional Rings in a Three-Dimensional Dissipative Cold Atomic Gas, Phys. Rev. Lett. **118**, 045701 (2017).
[25] R. Kolkowski, S. Kovaios, and A. F. Koenderink, Pseudochirality at exceptional rings of optical metasurfaces, Phys. Rev. Res. **3**, 023185 (2021).
[26] R. A. V. Poblete, Photonic flat band dynamics, Adv. Phys.: X **6**, 1878057 (2021).
[27] I. L. Garanovich, S. Longhi, A. A. Sukhorukov, and Y. S. Kivshar, Light propagation and localization in modulated photonic lattices and waveguides, Phys. Rep. **518**, 1 (2012).
[28] S. Longhi, M. Marangoni, M. Lobino, R. Ramponi, and P. Laporta, Observation of Dynamic Localization in Periodically Curved Waveguide Arrays, Phys. Rev. Lett. **96**, 243901 (2006).
[29] T. Biesenthal, M. Kremer, M. Heinrich, and A. Szameit, Experimental Realization of PT-Symmetric Flat Bands, Phys. Rev. Lett. **123**, 183601 (2019).
[30] R. A. Vicencio, C. Cantillano, L. Morales-Inostroza, B. Real, C. Mejía-Cortés, S. Weimann, A. Szameit, and M. I. Molina, Observation of Localized States in Lieb Photonic Lattices, Phys. Rev. Lett. **114**, 245503 (2015).
[31] S. Mukherjee, A. Spracklen, D. Choudhury, N. Goldman, P. Öhberg, E. Andersson, and R. R. Thomson, Observation of a Localized Flat-Band State in a Photonic Lieb Lattice, Phys. Rev. Lett. **114**, 245504 (2015).
[32] P. Wang, Y. Zheng, X. Chen, C. Huang, Y. V. Kartashov, L. Torner, V. V. Konotop, and F. Ye, Localization and delocalization of light in photonic moiré lattices, Nature (London) **577**, 42 (2020).
[33] M. Xiao, Y. Li, S. Jin, and J. Gea-Banacloche, Measurement of Dispersive Properties of Electromagnetically Induced Transparency in Rubidium Atoms, Phys. Rev. Lett. **74**, 666 (1995).
[34] Z. Zhang, R. Wang, Y. Zhang, Y. V. Kartashov, F. Li, H. Zhong, H. Guan, K. Gao, F. L. Li, Y. Zhang, and M. Xiao, Observation of edge solitons in photonic graphene, Nat. Commun. **11**, 1902 (2020).
[35] Z. Zhang, F. Li, G. Malpuech, Y. Zhang, O. Bleu, S. Koniakhin, C. Li, Y. Zhang, M. Xiao, and D. D. Solnyshkov, Particlelike Behavior of Topological Defects in Linear Wave Packets in Photonic Graphene, Phys. Rev. Lett. **122**, 233905 (2019).
[36] Z. Zhang, Y. Feng, F. Li, S. Koniakhin, C. Li, F. Liu, Y. Zhang, M. Xiao, G. Malpuech, and D. Solnyshkov, Angular-Dependent Klein Tunneling in Photonic Graphene, Phys. Rev. Lett. **129**, 233901 (2022).
[37] N. J. van Druten, S. S. R. Oemrawsingh, Y. Lien, C. Serrat, M. P. van Exter, and J. P. Woerdman, Observation of transverse modes in a microchip laser with combined gain and index guiding, J. Opt. Soc. Am. B **18**, 1793 (2001).
[38] Y-Q. Li and M. Xiao, Transient properties of an electromagnetically induced transparency in three-level atoms, Opt. Lett. **20**, 1489 (1995).
[39] See Supplemental Material at http://link.aps.org/supplemental/10.1103/PhysRevLett.131.013802 for more details on the experimental settings; calculation of susceptibility distribution from the density matrix method; the imaginary part of the band structure and its filtering effect; comparison of wave dynamics for different excitations in $\boldsymbol{k}$ space; and the energy exchange results from simulation and tight-binding model, which includes Refs. [40–42].
[40] G. Cáceres-Aravena, B. Real, D. Guzmán-Silva, A. Amo, L. E. F. Foa Torres, and R. A. Vicencio, Experimental observation of edge states in SSH-Stub photonic lattices, Phys. Rev. Res. **4**, 013185 (2022).
[41] D. Leykam, O. Bahat-Treidel, and A. S. Desyatnikov, Pseudospin and nonlinear conical diffraction in Lieb lattices, Phys. Rev. A **86**, 031805(R) (2012).
[42] J. Ma, J.-W. Rhim, L. Tang, S. Xia, H. Wang, X. Zheng, S. Xia, D. Song, Y. Hu, Y. Li, B.-J. Yang, D. Leykam, and Z. Chen, Direct Observation of Flatband Loop States Arising from Nontrivial Real-Space Topology, Phys. Rev. Lett. **124**, 183901 (2020).
[43] Z. Zhang, Y. Feng, S. Ning, G. Malpuech, D. D. Solnyshkov, Z. Xu, Y. Zhang, and M. Xiao, Imaging lattice switching with Talbot effect in reconfigurable non-Hermitian photonic graphene, Photonics Res. **10**, 958 (2022).

[44] H. Kang, L. Wen, and Y. Zhu, Normal or anomalous dispersion and gain in a resonant coherent medium, Phys. Rev. A **68**, 063806 (2003).
[45] O. Bleu, G. Malpuech, and D. D. Solnyshkov, Robust quantum valley Hall effect for vortices in an interacting bosonic quantum fluid, Nat. Commun. **9**, 3991 (2018).
[46] A. Szameit, M. C. Rechtsman, O. Bahat-Treidel, and M. Segev, PT-symmetry in honeycomb photonic lattices, Phys. Rev. A **84**, 021806(R) (2011).
[47] J. Liu, Zh. Li, Z.-G. Chen, W. Tang, A. Chen, B. Liang, G. Ma, and J. Cheng, Experimental Realization of Weyl Exceptional Rings in a Synthetic Three-Dimensional Non-Hermitian Phononic Crystal, Phys. Rev. Lett. **129**, 084301 (2022).
[48] V. Boyer, C. F. McCormick, E. Arimondo, and P. D. Lett, Ultraslow Propagation of Matched Pulses by Four-Wave Mixing in an Atomic Vapor, Phys. Rev. Lett. **99**, 143601 (2007).
[49] Z. Zhang, S. Ning, H. Zhong, M. R. Belić, Y. Zhang, Y. Feng, S. Liang, Y. Zhang, and M. Xiao, Experimental demonstration of optical Bloch oscillation in electromagnetically induced photonic lattices, Fundam. Res. **2**, 401 (2022).
[50] I. M. Uzunov, R. Muschall, M. Gölles, Y. S. Kivshar, B. A. Malomed, and F. Lederer, Pulse switching in nolinear fiber directional couplers, Phys. Rev. E **51**, 2527 (1995).
[51] S. Raghavan, A. Smerzi, S. Fantoni, and S. R. Shenoy, Coherent oscillations between two weakly coupled Bose-Einstein condensates: Josephson effects, π oscillations, and macroscopic quantum self-trapping, Phys. Rev. A **59**, 620 (1999).
[52] M. Albiez, R. Gati, J. Fölling, S. Hunsmann, M. Cristiani, and M. K. Oberthaler, Direct Observation of Tunneling and Nonlinear Self-Trapping in a Single Bosonic Josephson Junction, Phys. Rev. Lett. **95**, 010402 (2005).
[53] Yu. A. Kosevich, L. I. Manevitch, and A. V. Savin, Wandering breathers and self-trapping in weakly coupled nonlinear chains: Classical counterpart of macroscopic tunneling quantum dynamics, Phys. Rev. E **77**, 046603 (2008).
[54] M. Król, I. Septembre, P. Oliwa, M. Kędziora, K. Łempicka-Mirek, M. Muszyński, R. Mazur, P. Morawiak, W. Piecek, P. Kula, W. Bardyszewski, P. G. Lagoudakis, D. D. Solnyshkov, G. Malpuech, B. Piętka, and J. Szczytko, Annihilation of exceptional points from different Dirac valleys in a 2D photonic system, Nat. Commun. **13**, 5340 (2022).
[55] J. Wiersig, Enhancing the Sensitivity of Frequency and Energy Splitting Detection by Using Exceptional Points: Application to Microcavity Sensors for Single-Particle Detection, Phys. Rev. Lett. **112**, 203901 (2014).
[56] J.-H. Park, A. Ndao, W. Cai, L. Hsu, A. Kodigala, T. Lepetit, Y.-H. Lo, and B. Kanté, Symmetry-breaking- induced plasmonic exceptional points and nanoscale sensing, Nat. Phys. **16**, 462 (2020).
[57] J. Wiersig, Response strengths of open systems at exceptional points, Phys. Rev. Res. **4**, 023121 (2022).
[58] S. Karbasi, R. J. Frazier, K. W. Koch, T. Hawkins, J. Ballato, and A. Mafi, Image transport through a disordered optical fiber mediated by transverse Anderson localization, Nat. Commun. **5**, 3362 (2014).